

Predictive Simulations and Optimization of Nanowire Field-Effect PSA Sensors Including Screening

Stefan Baumgartner,¹ Clemens Heitzinger,^{1,2}
Aleksandar Vacic,^{3,4} and Mark A. Reed³

¹ AIT Austrian Institute of Technology, Donau-City-Strasse 1, 1220 Vienna, Austria.

² Department of Applied Mathematics and Theoretical Physics (DAMTP),
University of Cambridge, Wilberforce Road, Cambridge CB3 0WA, United Kingdom.

³ Departments of Electrical Engineering and Applied Physics, Yale University,
15 Prospect Street, New Haven, Connecticut 06511, United States.

⁴ 1366 Technologies, Inc., 6 Preston Ct., Bedford, Massachusetts 01730, United
States.

E-mail: Stefan.Baumgartner@univie.ac.at, C.Heitzinger@damtp.cam.ac.uk,
Alek.Vacic@gmail.com, Mark.Reed@yale.edu

Abstract. We apply our self-consistent PDE model for the electrical response of field-effect sensors to the 3D simulation of nanowire PSA (prostate-specific antigen) sensors. The charge concentration in the biofunctionalized boundary layer at the semiconductor-electrolyte interface is calculated using the PROPKA algorithm, and the screening of the biomolecules by the free ions in the liquid is modeled by a sensitivity factor. This comprehensive approach yields excellent agreement with experimental current-voltage characteristics without any fitting parameters. Having verified the numerical model in this manner, we study the sensitivity of nanowire PSA sensors by changing device parameters, making it possible to optimize the devices and revealing the attributes of the optimal field-effect sensor.

1. Introduction

Nanowire field-effect sensors are appealing sensing devices with a wide range of applications [1–11]. In recent years, direct detection of proteins from whole blood has been demonstrated experimentally, [12] including the detection of PSA a short while ago [13]. Sensors of antigen-antibody type, such as PSA sensors, consist of nanowires functionalized with antibodies at the surface. The sensor surface is then exposed to an aqueous solution containing antigens, and when the antigens bind to the antibodies, the partial charges of the antigen-antibody complex result in an electrostatic field effect. This effect is similar to a gate electrode in a transistor. Consequently, the current of electrons and holes through the semiconducting nanowires is modulated by the field effect and makes it possible to quantify the target molecules [14–20]. The advantages of nanowire devices for sensing applications are their high sensitivity, the selectivity of the functionalization, their label-free operation, and their ability to sense in real time [3, 8, 21]. They can also be fabricated in a CMOS compatible fashion [7].

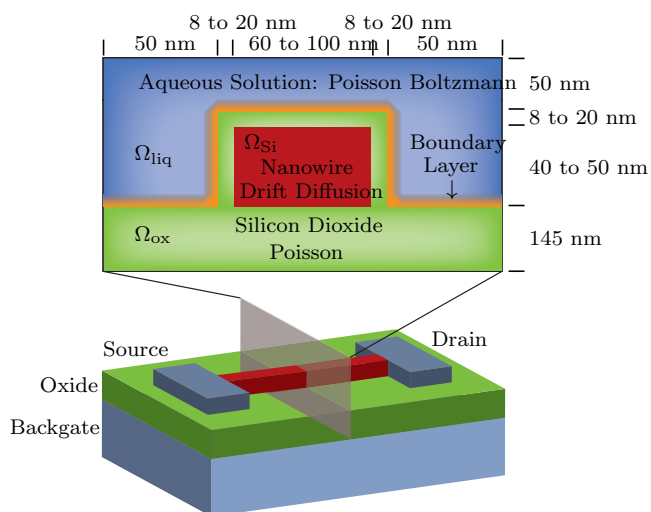


Figure 1. Schematic diagram of the nanowire field-effect PSA sensors investigated here.

Despite the experimental progress in the past few years, physics based modeling of the detection mechanism and quantitative understanding including all charges in the system has been missing. Mathematical modeling and simulation using 3D systems of partial differential equations (PDEs) [20, 22–24] has the advantage that all physically relevant quantities such as the electrostatic potential, the electron density, and the hole density are calculated self-consistently throughout the device including the biofunctionalized boundary layer. Having solved the equations, the current-voltage characteristics and the sensitivity can be determined immediately, and the behavior of the sensors can be studied by varying device parameters. Although the applied backgate voltage has a crucial influence on sensitivity, it is found that there is also a

strong interdependence between the parameters, which can be studied with our model.

This paper is organized as follows. First, we describe the two parts of the model, i.e., the macroscopic part (which includes the nanowire device, the substrate, and the electrolyte) and the microscopic part (which includes the biofunctionalized surface layer and the screening of the biomolecules by free ions). These two parts are connected by a self-consistent iteration. Using the device geometry shown in Figure 1, we verified the numerical model by comparing the simulations of the biofunctionalized surface layer and the electrical response of the device with experimental data. We note that there are no fitting parameters. The sensitivity of the sensors in terms of the applied voltages, the doping concentration, and the geometry is discussed in the last section, which also identifies pathways to optimal sensors and concludes the paper.

2. The Model

2.1. The Macroscopic Model

The domain Ω as depicted in Figure 1 is partitioned into three subdomains Ω_{Si} , Ω_{ox} , and Ω_{liq} corresponding to the three materials silicon, silicon oxide, and the liquid. The silicon nanowire is always covered by a thin layer of silicon oxide and surrounded by the liquid containing the target molecules, i.e., antigens in our case. At the interface Γ between the silicon oxide and the liquid, the charge concentration exhibits a rapidly oscillating spatial structure which leads to a multiscale problem [22]. In the following, the x -direction is always normal to the interface Γ located at $x = 0$ for notational convenience.

The basic equation for the electrostatic potential is the Poisson equation

$$-\nabla \cdot (\varepsilon(x, y, z) \nabla V(x, y, z)) = \rho(x, y, z) \quad \text{in } \Omega, \quad (1a)$$

$$V(0+, y, z) = V(0-, y, z) \quad \text{on } \Gamma, \quad (1b)$$

$$\varepsilon_{\text{liq}} \partial_x V(0+, y, z) = \varepsilon_{\text{ox}} \partial_x V(0-, y, z) \quad \text{on } \Gamma, \quad (1c)$$

where V is the electrostatic potential, ρ is the charge concentration, and ε is the permittivity. The continuity conditions (1b) and (1c) are due to the jump in the permittivity ε between two different materials.

After homogenization of the rapidly oscillating charge concentration in the boundary layer [22], the Poisson equation becomes the effective system

$$-\nabla \cdot (\varepsilon(x, y, z) \nabla V(x, y, z)) = \rho(x, y, z) \quad \text{in } \Omega_{\text{Si}} \cup \Omega_{\text{ox}}, \quad (2a)$$

$$-\nabla \cdot (\varepsilon(x, y, z) \nabla V(x, y, z)) = 0 \quad \text{in } \Omega_{\text{liq}}, \quad (2b)$$

$$V(0+, y, z) - V(0-, y, z) = \frac{\alpha(y, z)}{\varepsilon_{\text{liq}}} \quad \text{on } \Gamma, \quad (2c)$$

$$\varepsilon_{\text{liq}} \partial_x V(0+, y, z) - \varepsilon_{\text{ox}} \partial_x V(0-, y, z) = -\gamma(y, z) \quad \text{on } \Gamma, \quad (2d)$$

where $0+$ denotes the limit at the interface on the side of the liquid, while $0-$ is the limit on the side of the silicon-oxide layer. The two interface conditions (2c) and (2d) mean that the rapidly oscillating charge concentration in the surface layer is described by

the macroscopic dipole-moment density α and the macroscopic surface-charge density γ after homogenization. The computational significance of the homogenized equation (2) and the interface conditions is that the cumulative effect of the boundary layer can be included in device-level simulations without the need to resolve the molecules in the computational grid, thus decreasing the computational effort by orders of magnitude.

The charge concentration in the boundary layer and hence both the values of γ and α are computed by PROPKA simulations for the biomolecules in question as described below.

We now model the semiconductor. In Ω_{Si} , the drift-diffusion-Poisson system

$$-\nabla \cdot (\varepsilon_{\text{Si}} \nabla V) = q(p - n + C_{\text{dop}}), \quad (3a)$$

$$\nabla \cdot J_n = R(n, p), \quad (3b)$$

$$\nabla \cdot J_p = -R(n, p), \quad (3c)$$

$$J_n = D_n \nabla n - \mu_n n \nabla V, \quad (3d)$$

$$J_p = -D_p \nabla p - \mu_p p \nabla V, \quad (3e)$$

describes the transport of electrons and holes. Here q is the elementary charge, C_{dop} is the doping concentration, n is the electron concentration, p is the hole concentration, D_n and D_p are the electron and hole diffusion coefficients, μ_n and μ_p are their mobilities, J_n and J_p are their current densities, and R denotes the recombination rate [25]. Here we use the popular Shockley-Read-Hall recombination rate

$$R(n, p) := \frac{np - n_i^2}{\tau_p(n + n_i) + \tau_n(p + n_i)}, \quad (4)$$

where n_i denotes the intrinsic charge density and τ_n and τ_p are the relaxation times of the electrons and holes, respectively. Furthermore, the Einstein relations $D_n = U_T \mu_n$ and $D_p = U_T \mu_p$ are assumed to hold, where U_T is the thermal voltage.

The liquid Ω_{liq} is described by the Poisson-Boltzmann equation

$$-\nabla \cdot (\varepsilon_{\text{liq}} \nabla V) = \sum_{\sigma \in \{-1, 1\}} \eta \sigma \exp(-\sigma \beta V), \quad (5)$$

where η is the ionic bulk concentration and the constant β is defined as $\beta := q/(kT)$, where k is the Boltzmann constant and T is the temperature. The right-hand side of equation (5) is the sum over all valences σ of ion species so that the set $\{-1, 1\}$ corresponds to a 1:1 electrolyte such as Na^+Cl^- , for example.

At the source, drain, and back-gate contacts, Dirichlet boundary conditions

$$V|_{\partial\Omega_S} = V_S, \quad n|_{\partial\Omega_S} = n_S, \quad p|_{\partial\Omega_S} = p_S, \quad (6a)$$

$$V|_{\partial\Omega_D} = V_D, \quad n|_{\partial\Omega_D} = n_D, \quad p|_{\partial\Omega_D} = p_D, \quad (6b)$$

$$V|_{\partial\Omega_G} = V_G \quad (6c)$$

hold, as well as at the electrode in the liquid if one is present [26]. Zero Neumann boundary conditions are used everywhere else.

2.2. The Microscopic Model

In order to calculate the charge of PSA, we use the structure from the Protein Data Bank (see the left-hand part of Figure 2) and compute the charge state of the protein by using the PROPKA algorithm [27–30]. The charge of PSA as a function of pH value obtained in that manner is shown in the right-hand part of Figure 2.

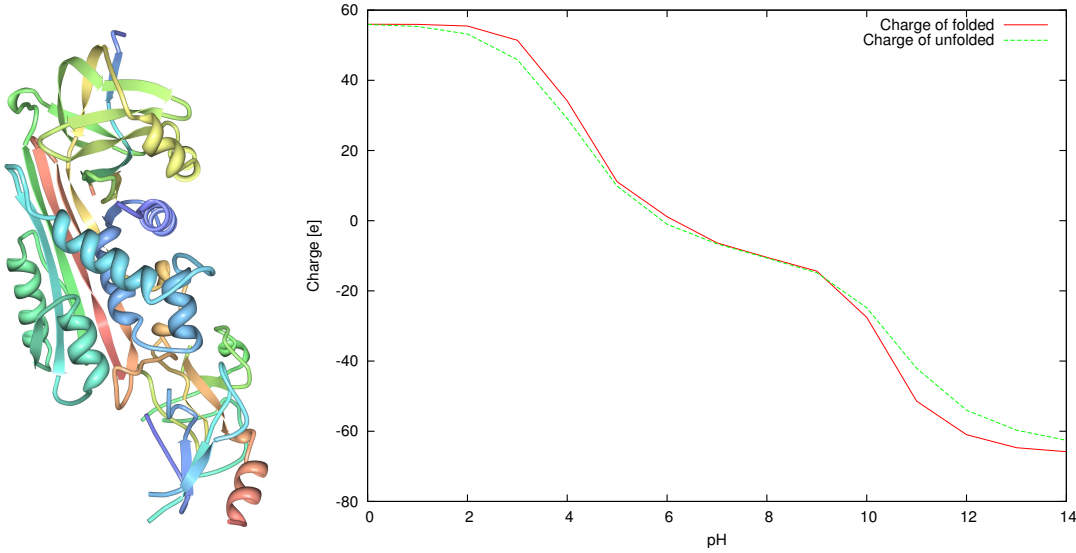


Figure 2. Left: Structure of protein 1ezx from the Protein Data Bank (<http://www.pdb.org/pdb/explore/explore.do?pdbId=1ezx>) with primary citation [31]. Right: Charge of protein 1EZx as a function of pH value and as calculated by PROPKA (<http://propka.ki.ku.dk/>).

Since we compare the simulations with measurements performed at a pH value of 9 below, we note a total charge of PSA -15 q at this pH value. Using a footprint of 10 nm for the functionalized molecules, which is achievable in experiments [32], this results in an unscreened surface charge of $-1.5\text{ q} \cdot \text{nm}^{-2}$.

2.3. Screening

The liquid surrounding the nanowire sensors is an ionic solution. Therefore, the effective charge of the biomolecules giving rise to the field effect is clearly lowered due to Debye screening [33]. The screening decreases exponentially with distance. More precisely, it decreases as $\exp(-x/\lambda_D)$, where the Debye length λ_D is defined as

$$\lambda_D := \frac{1}{\sqrt{4\pi l_B \sum_i \rho_i z_i^2}}. \quad (7)$$

Here $l_B = 0.7\text{ nm}$ is the Bjerrum length, and ρ_i and z_i are the concentration and valence of the ion species i .

Assuming the protein to be a point charge at a distance l from the nanowire surface, i.e., we can model Debye screening by using a sensitivity factor describing the induced change due to screening between 0 and 1. This sensitivity factor is given by

$$\Gamma_l \approx 2 \frac{r}{r+l} \left(1 + \sqrt{\frac{r}{r+l}} \exp\left(\frac{l}{\lambda_D}\right) \right)^{-1} \quad (8)$$

for a radial nanowire with radius r [34]. This model has been used for the simulation of nanowire sensors in [35]. In the case of a planar nanoribbon nanowire, we obtain the sensitivity factor

$$\Gamma_l \approx 2 \left(1 + \exp\left(\frac{l}{\lambda_D}\right) \right)^{-1} \quad (9)$$

for $r \rightarrow \infty$ (see also [13]).

For antibody-antigen sensors using a functionalization with anti-CA15-3 (CA15-3 is cancer antigen 15-3), this value is $\approx 50\%$ for C-termini functionalized antibodies when using a 1 mM bicarbonate sensing buffer and $\approx 65\%$ when using N-terminal functionalization (for a detailed discussion see [13]). Hence the resulting screened surface charge of PSA at a pH value of 9 and a C-terminal functionalized antibody is around $-0.75 \text{ q} \cdot \text{nm}^{-2}$.

The Self-Consistent Loop

We can now compute the electrostatic potential V and the concentrations of the charge carriers n and p in a self-consistent loop. After choosing initial values n_0 , p_0 , α_0 , and γ_0 , the following steps are performed in a Scharfetter-Gummel type iteration scheme.

- (i) In iteration $k + 1$, solve the homogenized boundary-value problem

$$\begin{aligned} -\varepsilon_{\text{Si}} \Delta V_{k+1} &= q(C_{\text{dop}} + p_k - n_k) && \text{in } \Omega_{\text{Si}}, \\ -\varepsilon_{\text{ox}} \Delta V_{k+1} &= 0 && \text{in } \Omega_{\text{ox}}, \\ -\varepsilon_{\text{liq}} \Delta V_{k+1} &= \sum_{\sigma \in \{-1,1\}} \eta \sigma e^{-\sigma \beta V_{k+1}} && \text{in } \Omega_{\text{liq}}, \\ V_{k+1}(0+) &- V_{k+1}(0-) = \frac{\alpha_k}{\varepsilon(0+)} && \text{on } \Gamma, \\ \varepsilon_{\text{liq}} \nabla V_{k+1}(0+) - \varepsilon_{\text{ox}} \nabla V_{k+1}(0-) &= -\gamma_k && \text{on } \Gamma, \\ V_{k+1} &= V_D && \text{on } \partial\Omega_D, \\ \nabla_\nu V_{k+1} &= 0 && \text{on } \partial\Omega_N \end{aligned}$$

to obtain the electrostatic potential V_{k+1} .

- (ii) Then solve the boundary-value problem

$$\begin{aligned} \nabla \cdot (D_n \nabla n_{k+1} - \mu_n n_{k+1} \nabla V_k) &= R(n_{k+1}, p_k) && \text{in } \Omega_{\text{Si}}, \\ n_{k+1} &= n_D && \text{on } \partial\Omega_D, \\ \nabla_\nu n_{k+1} &= 0 && \text{on } \partial\Omega_N \end{aligned}$$

to obtain the electron concentration n_{k+1} .

(iii) Then solve the boundary-value problem

$$\begin{aligned} \nabla \cdot (D_p \nabla p_{k+1} - \mu_p p_{k+1} \nabla V_k) &= R(n_{k+1}, p_{k+1}) && \text{in } \Omega_{\text{Si}}, \\ p_{k+1} &= p_D && \text{on } \partial\Omega_D, \\ \nabla_\nu p_{k+1} &= 0 && \text{on } \partial\Omega_N \end{aligned}$$

to obtain the hole concentration p_{k+1} .

(iv) Compute $\alpha_{k+1} = \alpha(V_{k+1})$ and $\gamma_{k+1} = \gamma(V_{k+1})$ or look up the values in a precomputed table.

(v) Increase k and go to the first step.

The existence, local uniqueness around thermal equilibrium, and smoothness of the solution (V, n, p) have been shown based on a fixed-point theorem and the inverse-function theorem [23].

3. Numerical Results: Model Validation and Device Optimization

3.1. Model Verification

As aforementioned, we simulate a sensor with the basic geometry depicted in Figure 1. The length of the nanowire is 1000 nm, the doping concentration is -10^{16} cm^{-3} , and the source voltage is $V_S = -0.2 \text{ V}$. In the structures fabricated, the thickness of the silicon nanowire can vary between approximately 40 nm and 50 nm and the thickness of the silicon dioxide can vary between 8 nm and 20 nm.

Knowing the geometry, it is possible to extract the electron and hole mobilities and the thermal voltage by comparison with the measured current-voltage characteristics. This is required, because silicon nanowires with such a high surface-to-volume ratio cannot be expected to have bulk properties, e.g., due to surface-roughness effects. Therefore the slope of the current-voltage characteristics and the gap between the characteristics of nanowires of different widths are used to determine the physical properties of the nanowire sensors.

Table 1. Device parameters used in Figure 3.

	Top-oxide thickness	Nanowire thickness	Hole mobility	Thermal voltage
(a)	8 nm	50 nm	$100 \text{ cm}^{-2} \text{ V}^{-1} \text{ s}^{-1}$	0.021 V
(b)	14 nm	50 nm	$50 \text{ cm}^{-2} \text{ V}^{-1} \text{ s}^{-1}$	0.023 V
(c)	8 nm	40 nm	$220 \text{ cm}^{-2} \text{ V}^{-1} \text{ s}^{-1}$	0.021 V
(d)	14 nm	40 nm	$50 \text{ cm}^{-2} \text{ V}^{-1} \text{ s}^{-1}$	0.023 V

The physical parameters determined in this manner are shown in Table 1 and the corresponding agreement between measurement and simulation is shown in Figure 3. In Figure 3(a), simulated and measured current-voltage characteristics of two devices

with 60 nm and 100 nm wide nanowires, each with a 8 nm thick top oxide, a nanowire thickness of 50 nm, a hole mobility of $100 \text{ cm}^{-2}\text{V}^{-1}\text{s}^{-1}$, and a thermal voltage of 0.021 V, are shown. We note that there is a substantial difference in the hole mobilities (up to 4 times larger). Due to loss of convergence of the Scharfetter-Gummel iteration for large negative gate voltages, the current-voltage characteristics are calculated only up to a certain gate voltage. This is due to the fact that the solutions of the drift-diffusion-Poisson system are unique only for applied voltages sufficiently close to thermal equilibrium [23].

The simulations with the other parameters in rows (b), (c), and (d) in Table 1 were compared to the current-voltage characteristic of the device with a 100 nm wide nanowire as well, while it is found that the agreement for the 60 nm wide nanowire is always worse (see Figure 3(b-d)). This implies that row (a) in Table 1 contains the correct parameters for the real-world device. This can be further validated by comparing the measured sensitivity of the sensor with simulated sensitivity values.

In the next step, we therefore consider the sensitivity of the devices in Figure 3 with the parameters in Table 1 and vary the screened surface charge γ between $-0.4 \text{ q} \cdot \text{nm}^{-2}$ and $-0.8 \text{ q} \cdot \text{nm}^{-2}$ as an additional free parameter. The results are shown in Figure 4. As expected, the best agreement with the measured sensitivity is found using the best parameters for the current-voltage characteristics, i.e., the slope when changing from 60 nm to 100 nm wide nanowires is nearly the same and the corresponding screened surface charge is in the range of the screened surface charge computed by PROPKA. To be more specific, the devices with a 14 nm thick top oxide (see (b) and (d) in Figure 4) have the same slope when changing from 60 nm wide nanowires to 100 nm wide nanowires, but then the screened surface charge is higher than the unscreened surface charge computed by PROPKA. Therefore this oxide thickness cannot be realistic. For the devices with a 8 nm thick top oxide and a 40 nm thick nanowire, the slope does not match the measured sensitivity, and the corresponding screened surface charge for 60 nm wide nanowires is higher than the unscreened surface charge computed by PROPKA. Therefore this case is also not realistic.

This implies that parameter set (a) in Table 1 is the best. In the following we therefore consider the device with a 8 nm thick top oxide, a 50 nm thick nanowire, a hole mobility of $100 \text{ cm}^{-2}\text{V}^{-1}\text{s}^{-1}$, and a thermal voltage of 0.021 V, for which the agreement between measurements and simulations is very good both regarding the current-voltage characteristics (see (a) in Figure 3) and the sensitivity for a surface charge of $\gamma = -0.75 \text{ nm}^{-2}$ (see (a) in Figure 4).

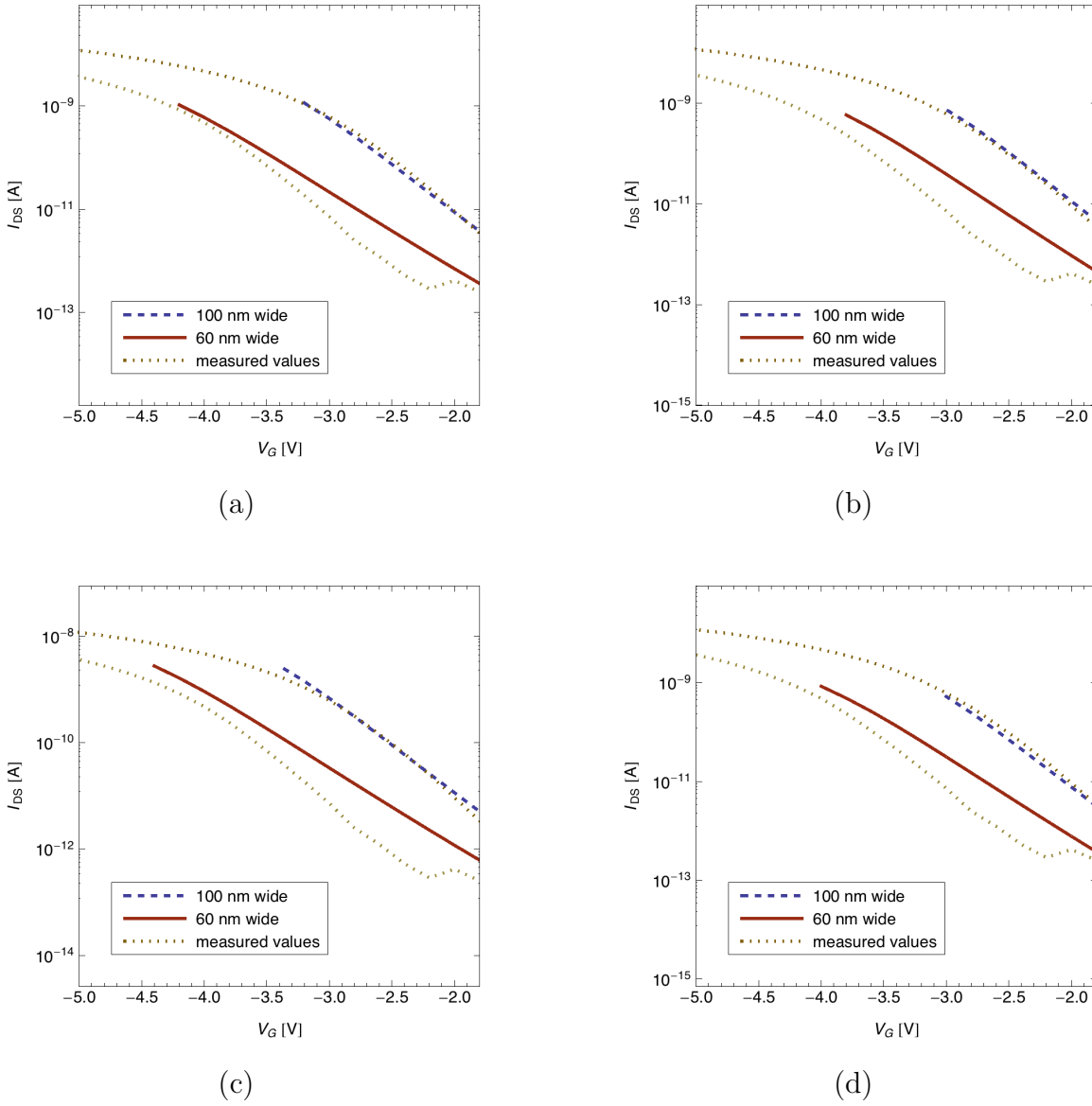
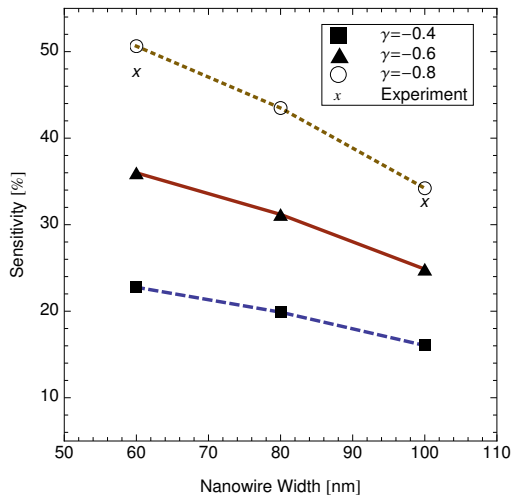


Figure 3. (a): Current-voltage characteristic for a nanowire device with a 60 nm and a 100 nm wide nanowire with 8 nm top oxide and 50 nm high silicon. The hole mobility is $100 \text{ cm}^2 \text{ V}^{-1} \text{ s}^{-1}$ and the thermal voltage is 0.021 V, corresponding to (a) from Table 1).

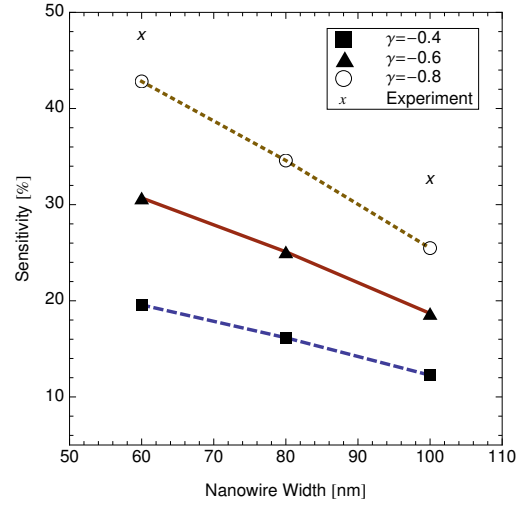
(b): Current-voltage characteristic for a nanowire device with a 60 nm and a 100 nm wide nanowire with 14 nm top oxide and 50 nm high silicon. The hole mobility is $50 \text{ cm}^2 \text{ V}^{-1} \text{ s}^{-1}$ and the thermal voltage is 0.023 V, corresponding to (b) from Table 1).

(c): Current-voltage characteristic for a nanowire device with a 60 nm and a 100 nm wide nanowire with 8 nm top oxide and 40 nm high silicon. The hole mobility is $220 \text{ cm}^2 \text{ V}^{-1} \text{ s}^{-1}$ and the thermal voltage is 0.021 V, corresponding to (c) from Table 1).

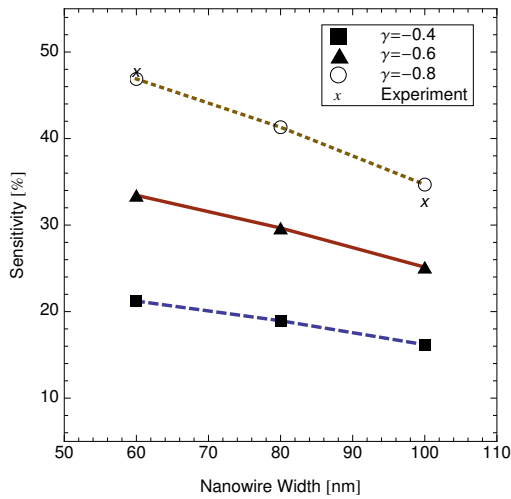
(d): Current-voltage characteristic for a nanowire device with a 60 nm and a 100 nm wide nanowire with 14 nm top oxide and 40 nm high silicon. The hole mobility is $50 \text{ cm}^2 \text{ V}^{-1} \text{ s}^{-1}$ and the thermal voltage is 0.023 V, corresponding to (d) from Table 1).



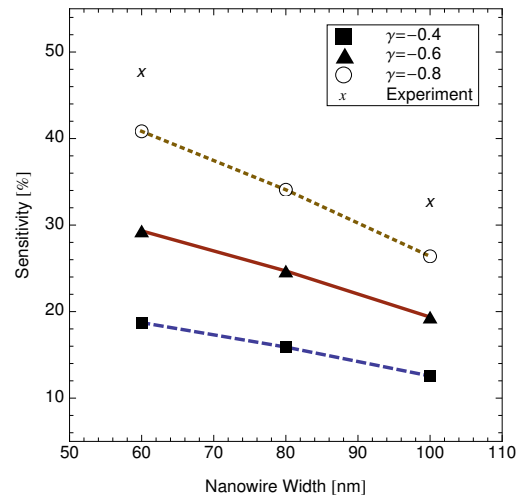
(a)



(b)



(c)



(d)

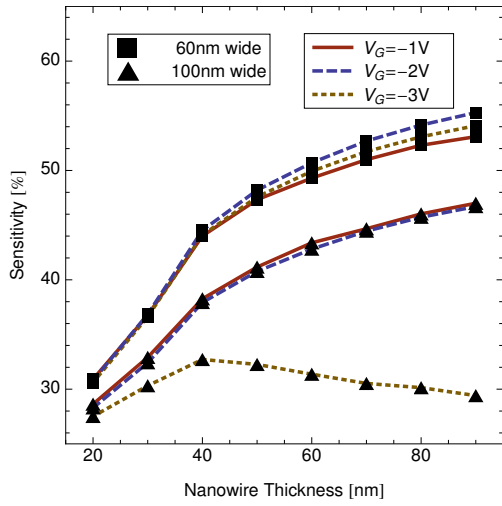
Figure 4. All subfigures: The sensitivity is shown for 60 nm, 80 nm, and 100 nm wide nanowires with a surface charge of $\gamma = -0.4 \text{ q} \cdot \text{nm}^{-2}$, $\gamma = -0.6 \text{ q} \cdot \text{nm}^{-2}$, and $\gamma = -0.8 \text{ q} \cdot \text{nm}^{-2}$. Measurements are shown as well.

(a): Sensitivity of a sensor with the same configuration used in Figure 3(a).

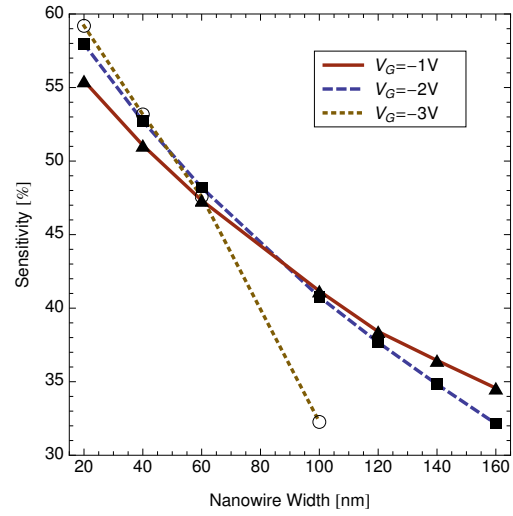
(b): Sensitivity of a sensor with the same configuration used in Figure 3(b).

(c): Sensitivity of a sensor with the same configuration used in Figure 3(c).

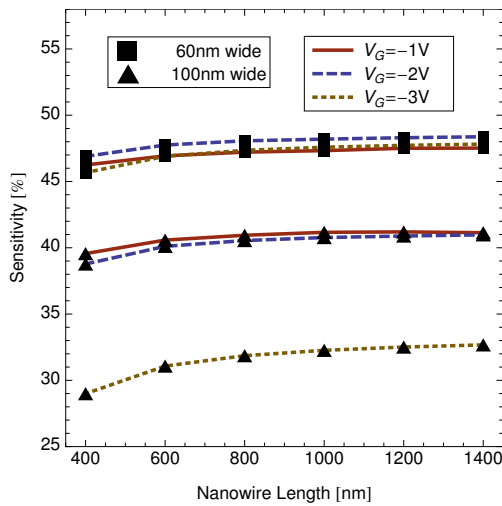
(d): Sensitivity of a sensor with the same configuration used in Figure 3(d).



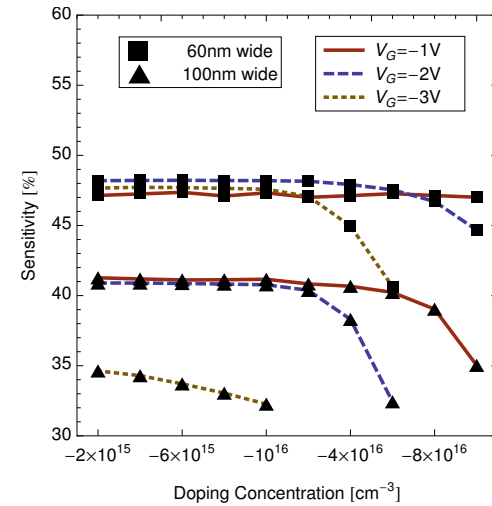
(a)



(b)

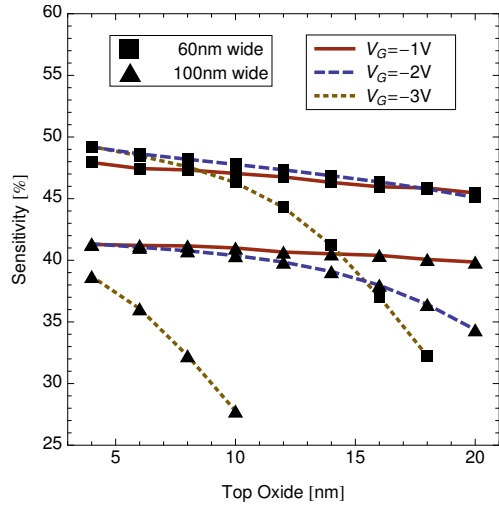


(c)

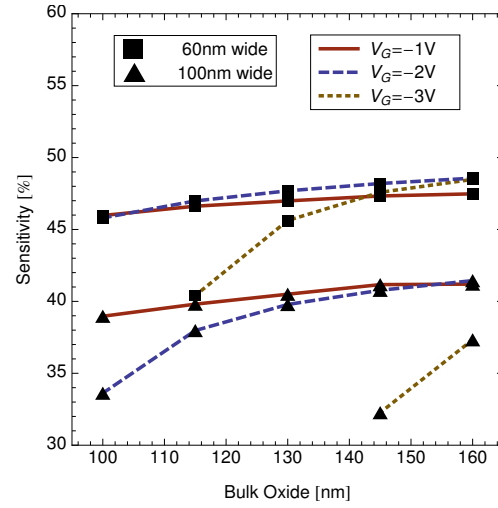


(d)

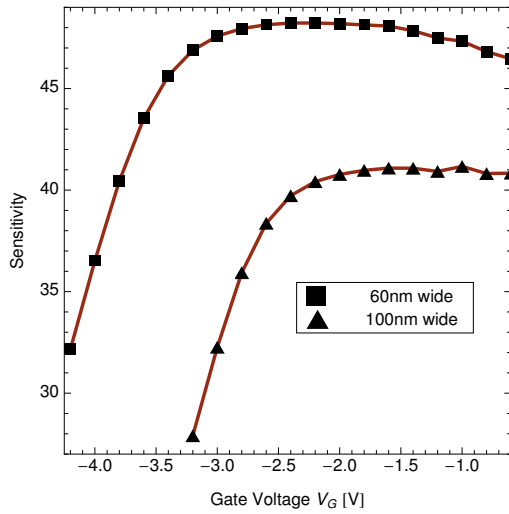
Figure 5. (a): Sensitivity as a function of nanowire thickness for a 60 nm and 100 nm wide nanowire and gate voltages $V_G = -1V$, $V_G = -2V$, and $V_G = -3V$. (b): Sensitivity as a function of nanowire width for a sensor with gate voltages of $V_G = -1V$, $V_G = -2V$, and $V_G = -3V$. (c): Sensitivity as a function of nanowire length for a 60 nm and 100 nm wide nanowire and gate voltages $V_G = -1V$, $V_G = -2V$, and $V_G = -3V$. (d): Sensitivity as a function of doping concentration for a 60 nm and 100 nm wide nanowire and gate voltages $V_G = -1V$, $V_G = -2V$, and $V_G = -3V$.



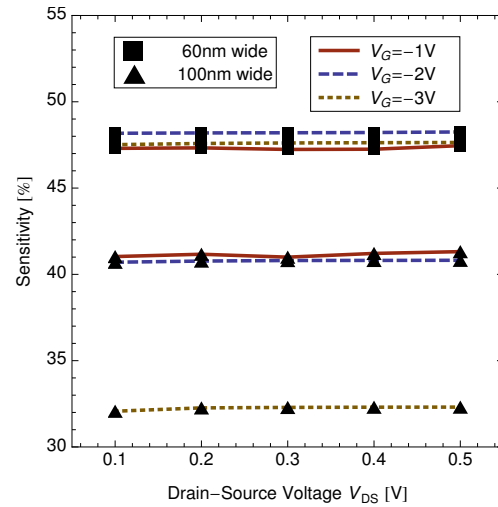
(a)



(b)



(c)



(d)

Figure 6. (a): Sensitivity as a function of top oxide for a 60 nm and 100 nm wide nanowire and gate voltages $V_G = -1$ V, $V_G = -2$ V, and $V_G = -3$ V. (b): Sensitivity as a function of bulk oxide for a 60 nm and 100 nm wide nanowire and gate voltages $V_G = -1$ V, $V_G = -2$ V, and $V_G = -3$ V. (c): Sensitivity as a function of gate voltage for a 60 nm and 100 nm wide nanowire. (d): Sensitivity as a function of drain-source voltage for a 60 nm and 100 nm wide nanowire and gate voltages $V_G = -1$ V, $V_G = -2$ V, and $V_G = -3$ V.

3.2. Sensitivity and Optimal Sensors

Having validated the model and the simulations using measurements, the device properties can be varied in order to optimize the sensors especially with respect to sensitivity. The simulations also make it possible to easily quantify the effect of changes in device parameters, to quantify the nonlinear dependencies between parameters such as the backgate voltage and the geometry of the nanowires, and to determine the optimal operating regime.

We first investigate how the sensitivity is influenced by different physical and geometric device properties. As aforementioned, the standard nanowire device considered here is 60 nm and 100 nm wide and 50 nm high. The first question is if the sensitivity can be improved by varying the doping concentration and the geometry, i.e., the thickness, width, and length of the nanowire at different gate-voltage levels (see Figure 5).

The sensitivity depends on both the thickness and the width of the nanowire as seen in Figure 5(a). Both the 60 nm and the 100 nm wide nanowires show that sensitivity dramatically decreases when the thickness becomes too small. The sensitivity is improved when the wires are thicker unless the gate voltage is too low. But a low gate voltage by itself does not necessarily decrease the sensitivity; in the case of narrow nanowires, we find that a low gate voltage increases the sensitivity (see Figure 5(b)).

The length of the nanowire only has a minor influence on the sensitivity. A small increase in sensitivity is found when the nanowires are longer as depicted in the bottom left of Figure 5. The doping concentration affects the sensitivity only at high levels of doping and reduces it (see Figure 5(c)). Here we find again a correlation between the decrease in the sensitivity and the magnitude of the gate voltage.

A gate voltage that is too negative becomes detrimental. In Figure 5, it is seen that a gate voltage of $V_G = -3\text{ V}$ is too large and decreases sensitivity. At this point, the large gate voltage is the major parameter affecting charge transport and the relatively much smaller influence of the molecules is not observed well anymore. This effect is more pronounced in the larger devices (100 nm wide and thicker than circa 50 nm). While the molecules at the surface are sufficient to affect the whole silicon nanowire in the smaller devices, their effect is limited to the Debye length. In the large nanowires, a substantial part is not affected noticeably by the molecules at the surface, but it can be affected by a large gate voltage. Hence the relative influence of the molecules decreases, meaning that the sensitivity decreases.

In Figure 6, the crucial influence of the gate voltage on sensitivity becomes clear as well. Since a high gate voltage has more influence on the charge carriers in the nanowire than the typical surface charge of biomolecules, the sensitivity decreases. This can also be understood as a screening effect, i.e., the influence of the backgate voltage on the electrons and holes in the nanowire screens the influence of the surface charge. The clearest examples are the thicknesses of the top oxide and the bulk oxide. In Figure 6(a), as the thickness of the top oxide increases, the molecules are farther away from

the transducer and their effect and hence the sensitivity decrease. In Figure 6(b), as the thickness of the bulk oxide increases, the gate contact is farther away from the transducer, and the detrimental influence of the highly negative gate voltage decreases. The impact of a high gate voltage is also seen in Figure 6(c). However, not all voltages applied to the device turn out to decrease the sensitivity: In the case of the source voltage, the sensitivity remains at a certain level as depicted in Figure 6(d). These numerical results underline the importance of back-gated devices and the nonlinear influence of the design parameters.

4. Conclusion

Field-effect sensors based on nanowires are promising devices for the detection of biomolecules due to their direct detection mechanism offering several advantages. As for every sensor, a crucial question is how to achieve the best sensitivity. 3D simulations of nanowire field-effect sensors using our PDE model were used to provide quantitative understanding of the various parameters affecting sensitivity and to show how the optimal sensitivity can be achieved in terms of device geometry, nanowire properties, and applied voltages.

Special attention has been given to the selective biofunctionalized boundary layer at the nanowire surface. We have used a comprehensive approach starting from the molecular structure of PSA, calculating its charge using the PROPKA algorithm, and using a screening factor to compute the effective surface-charge density. We have verified the simulated current-voltage characteristics by comparison with measurements. It is important to note that 3D charge-transport simulations are necessary for realistic calculations, as 2D calculations using cylindrical coordinates cannot include the backgate contact.

Field-effect sensors are much more complicated devices than field-effect transistors, since there are more device parameters that can be varied. The simulations elucidate the design of the optimal field-effect sensor by quantifying the influence of the various device parameters and their interdependencies. The backgate voltage turns out to have a crucial influence on the sensitivity of the sensor, but the strong nonlinear interdependence of all parameters must also be taken into account in the design of the sensors.

Acknowledgment

S.B. and C.H. acknowledge support by the FWF (Austrian Science Fund) project no. P20871-N13 and by the WWTF (Vienna Science and Technology Fund) project no. MA09-028. C.H. acknowledges support by award no. KUK-I1-007-43 funded by the King Abdullah University of Science and Technology (KAUST). A.V. and M.R. acknowledge support by the DTRA project no. HDTRA1-10-1-0037.

The simulator is available from the authors on request.

References

- [1] M.J. Schöning and A. Poghossian. Bio FEDs (field-effect devices): State-of-the-art and new directions. *Electroanal.*, 18(19–20):1893–1900, 2006.
- [2] Y. Cui, Q. Wei, H. Park, and C.M. Lieber. Nanowire nanosensors for highly sensitive and selective detection of biological and chemical species. *Science*, 293(5533):1289–1292, 2001.
- [3] J. Hahm and C.M. Lieber. Direct ultrasensitive electrical detection of DNA and DNA sequence variations using nanowire nanosensors. *Nano Lett.*, 4(1):51–54, 2004.
- [4] G. Zheng, F. Patolsky, Y. Cui, W.U. Wang, and C.M. Lieber. Multiplexed electrical detection of cancer markers with nanowire sensor arrays. *Nat. Biotechnol.*, 23(10):1294–1301, 2005.
- [5] F. Patolsky, B.P. Timko, G. Zheng, and C.M. Lieber. Nanowire-based nanoelectronic devices in the life sciences. *MRS Bull.*, 32(2):142–149, 2007.
- [6] N. Elfström, A.E. Karlström, and J. Linnros. Silicon nanoribbons for electrical detection of biomolecules. *Nano Lett.*, 8(3):945–949, 2008.
- [7] E. Stern, J.F. Klemic, D.A. Routenberg, P.N. Wyrembak, D.B. Turner-Evans, A.D. Hamilton, D.A. LaVan, T.M. Fahmy, and M.A. Reed. Label-free immunodetection with CMOS-compatible semiconducting nanowires. *Nature*, 445(7127):519–522, 2007.
- [8] E. Stern, E.R. Steenblock, M.A. Reed, and T.M. Fahmy. Label-free electronic detection of the antigen-specific T-cell immune response. *Nano Lett.*, 8(10):3310–3314, 2008.
- [9] B. Tian, T. Cohen-Karni, Q. Qing, X. Duan, P. Xie, and C.M. Lieber. Three-dimensional, flexible nanoscale field-effect transistors as localized bioprobes. *Science*, 329(5993):830–834, 2010.
- [10] H.K. Hunt and A.M. Armani. Label-free biological and chemical sensors. *Nanoscale*, 2(9):1544–1559, 2010.
- [11] M. Swierczewska, G. Liu, S. Lee, and X. Chen. High-sensitivity nanosensors for biomarker detection. *Chemical Society Reviews*, 41(7):2641–2655, 2012.
- [12] E. Stern, A. Vacic, N.K. Rajan, J.M. Criscione, J. Park, B.R. Ilic, D.J. Mooney, M.A. Reed, and T.M. Fahmy. Label-free biomarker detection from whole blood. *Nat. Nanotechnol.*, 5(2):138–142, 2010.
- [13] Aleksandar Vacic, Jason M. Criscione, Nitin K. Rajan, Eric Stern, Tarek M. Fahmy, and Mark A. Reed. Determination of molecular configuration by debye length modulation. *J. Am. Chem. Soc.*, 133(35):13886–13889, 2011.
- [14] Clemens Heitzinger and Gerhard Klimeck. Computational aspects of the three-dimensional feature-scale simulation of silicon-nanowire field-effect sensors for DNA detection. *J. Comput. Electron.*, 6(1-3):387–390, 2007.
- [15] F.S. Zhou and Q.H. Wei. Scaling laws for nanoFET sensors. *Nanotechnology*, 19:015504, 2008.
- [16] Y. Liu and R.W. Dutton. Effects of charge screening and surface properties on signal transduction in field effect nanowire biosensors. *Journal of Applied Physics*, 106(1):014701–014701, 2009.
- [17] Clemens Heitzinger, Yang Liu, Norbert J. Mauser, Christian Ringhofer, and Robert W. Dutton. Calculation of fluctuations in boundary layers of nanowire field-effect biosensors. *J. Comput. Theor. Nanosci.*, 7(12):2574–2580, 2010.
- [18] A. Schulze, T. Hantschel, P. Eyben, AS Verhulst, R. Rooyackers, A. Vandooren, J. Mody, A. Nazir, D. Leonelli, and W. Vandervorst. Observation of diameter dependent carrier distribution in nanowire-based transistors. *Nanotechnology*, 22:185701, 2011.
- [19] C.C. Tsai, P.L. Chiang, C.J. Sun, T.W. Lin, M.H. Tsai, Y.C. Chang, and Y.T. Chen. Surface potential variations on a silicon nanowire transistor in biomolecular modification and detection. *Nanotechnology*, 22:135503, 2011.
- [20] Stefan Baumgartner, Martin Vasicek, and Clemens Heitzinger. Modeling and simulation of nanowire based field-effect biosensors. In G. Korotcenkov, editor, *Chemical Sensors: Simulation and Modeling*, pages 447–469. Momentum Press, 2012.
- [21] X.P.A. Gao, G. Zheng, and C.M. Lieber. Subthreshold regime has the optimal sensitivity for nanowire FET biosensors. *Nano Lett.*, 10(2):547–552, 2010.

- [22] C. Heitzinger, N. Mauser, and C. Ringhofer. Multiscale modeling of planar and nanowire field-effect biosensors. *SIAM J. Appl. Math.*, 70(5):1634–1654, 2010.
- [23] S. Baumgartner and C. Heitzinger. Existence and local uniqueness for 3d self-consistent multiscale models of field-effect sensors. *Commun. Math. Sci.*, 10(2):693–716, 2012.
- [24] S. Baumgartner, M. Vasicek, A. Bulyha, and C. Heitzinger. Optimization of nanowire DNA sensor sensitivity using self-consistent simulation. *Nanotechnology*, 22(42):425503/1–8, 2011.
- [25] P.A. Markowich, C.A. Ringhofer, and C. Schmeiser. *Semiconductor Equations*. Springer, Wien, 1990.
- [26] M.P. Lu, C.Y. Hsiao, W.T. Lai, and Y.S. Yang. Probing the sensitivity of nanowire-based biosensors using liquid-gating. *Nanotechnology*, 21(42):425505/1–5, 2010.
- [27] H. Li, A.D. Robertson, and J.H. Jensen. Very fast empirical prediction and rationalization of protein pKa values. *Proteins Struct. Funct. Bioinf.*, 61(4):704–721, 2005.
- [28] D.C. Bas, D.M. Rogers, and J.H. Jensen. Very fast prediction and rationalization of pKa values for protein–ligand complexes. *Proteins Struct. Funct. Bioinf.*, 73(3):765–783, 2008.
- [29] M.H.M. Olsson, C.R. Søndergaard, M. Rostkowski, and J.H. Jensen. PROPKA3: consistent treatment of internal and surface residues in empirical pKa predictions. *J. Chem. Theory Comput.*, 7(2):525–537, 2011.
- [30] C.R. Søndergaard, M.H.M. Olsson, M. Rostkowski, and J.H. Jensen. Improved treatment of ligands and coupling effects in empirical calculation and rationalization of pKa values. *J. Chem. Theory Comput.*, 7(7):2284–2295, 2011.
- [31] J.A. Huntington, R.J. Read, and R.W. Carrell. Structure of a serpin–protease complex shows inhibition by deformation. *Nature*, 407(6806):923–926, 2000.
- [32] Manuel Punzet, Dieter Baurecht, Franz Varga, Heidrun Karlic, and Clemens Heitzinger. Determination of surface concentrations of individual molecule-layers used in nanoscale biosensors by in-situ ATR-FTIR spectroscopy. *Nanoscale*, 4(7):2431–2438, 2012.
- [33] A. Bulyha and C. Heitzinger. An algorithm for three-dimensional Monte-Carlo simulation of charge distribution at biofunctionalized surfaces. *Nanoscale*, 3(4):1608–1617, 2011.
- [34] M.H. Sørensen, N.A. Mortensen, and M. Brandbyge. Screening model for nanowire surface-charge sensors in liquid. *Appl. Phys. Lett.*, 91(10):102105/1–3, 2007.
- [35] L. De Vico, L. Iversen, M.H. Sørensen, M. Brandbyge, J. Nygård, K.L. Martinez, and J.H. Jensen. Predicting and rationalizing the effect of surface charge distribution and orientation on nano-wire based FET bio-sensors. *Nanoscale*, 3(9):3635–3640, 2011.